THE JOURNAL OF PHYSICAL CHEMISTRY C
A JOURNAL OF THE AMERICAN CHEMICAL SOCIETY

pubs.acs.org/JPCC

Article

Reversible Switching of Molecular Conductance in Viologens is Controlled by the Electrochemical Environment

Jialing Li, Sanja Pudar, Hao Yu, Songsong Li, Jeffrey S. Moore, Joaquín Rodríguez-López, Nicholas E. Jackson, and Charles M. Schroeder*

Cite This: J. Phys. Chem. C 2021, 125, 21862–21872

Read Online

ACCESS | Metrics & More | Article Recommendations | Supporting Information

ABSTRACT: Charge transport in electrochemical energy-storage systems critically relies on supporting electrolytes to maintain ionic strength and solution conductivity. Despite recent progress, it is not fully understood how the solvation environment affects molecular charge transport of redox-active species near electrode interfaces. In this work, we characterize the charge-transport properties of bipyridinium molecules in a series of different supporting electrolyte and counterion environments using a combination of experiments and computational modeling. Interestingly, our results show that molecular charge transport in viologens critically depends on the chemical identity of counterions and the solvation environment. Using an electrochemical scanning tunneling microscope-break junction (ECSTM-BJ) instrument, we observe a large and reversible 10-fold enhancement in molecular conductance upon electrochemical reduction of the viologen redox pair ($V^{2+/+}$) to the radical cationic state in the electrolytic solution. Density functional theory (DFT) simulations show that charge transport is enhanced due to molecular conformational changes and planarization resulting from interactions with different counterions, which ultimately leads to enhanced charge transport in the reduced state. Overall, this work highlights the role of the counterion species on electrochemical charge transport in redox-active molecules that underpin the design of new energy-storage systems or programmable molecular electronic devices.

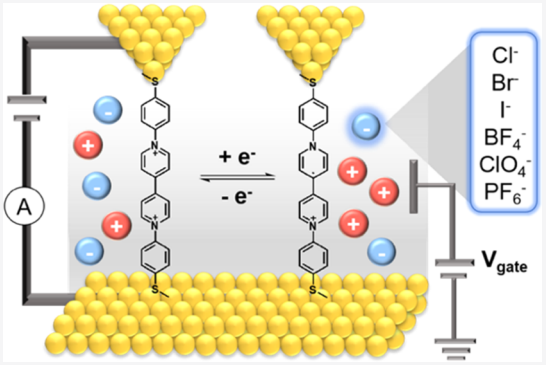

INTRODUCTION

The development of new energy-storage systems for next-generation batteries and smart electronic devices has attracted substantial scientific attention.[1,2] Designing energy-storage systems with enhanced performance requires a fundamental understanding of the charge-transport mechanisms in redox-active and conjugated organic molecules. Charge transport at the electrode−electrolyte interface involves multiple simultaneous and sequential steps such as intra- and interchain charge hopping via self-exchange,[3] charge diffusion with redox-active polymers or particles,[4] and charge transport between the redox groups and electrodes.[5,6] Molecular charge transport in these systems critically depends on the chemical identity of the redox-active moiety,[7] particle structure,[8] and the solvent[9] and supporting electrolyte.[10] Prior work has focused on understanding the role of different electrolyte species and electrode structures on interfacial charge transport. To this end, the physical and electrochemical properties of redox-active materials at electrode interfaces have been characterized using bulk-scale or microscopy-based methods such as scanning electrochemical microscopy (SECM),[11] atomic force microscopy (AFM),[12] and Raman spectroscopy.[13] Despite recent progress, we lack a full understanding of the charge-transport properties of redox-active molecules near electrode interfaces.

Recent advances in single-molecule characterization have enabled the study of charge-transport mechanisms in redox-active materials.[14] Prior work has focused on understanding intramolecular charge transport across a variety of materials with redox-active centers, including ferrocene,[15] anthraquinone,[16] viologen,[17] pyrrolotetrathiafulvalene,[18] hepta-aniline oligomers,[19] and naphthalocyanine.[20] Prior studies have shown that the molecular conductance and intrinsic charge-transport properties of redox-active molecules critically depend on the redox state.[21] Single-molecule techniques have also been used to explore the relationship between molecular charge transport and bulk electrochemical properties, revealing connections between molecular charge transport and redox potential[22] and interfacial charge-transfer kinetics.[23] In addition, redox-active and inactive molecules are also known to interact with the

Received: August 5, 2021
Revised: September 19, 2021
Published: October 5, 2021

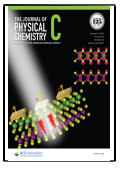

solvent and supporting electrolyte in complex electrochemical environments, thereby leading to changes in intra- and intermolecular charge transport.[24] In the context of redox-inactive molecules, single-molecule techniques have enabled understanding of the role of solvent on charge transport, revealing complexities in molecule−solvent interactions such as electrostatic interactions, chemical binding with the solvent,[25,26] and solvent binding to electrodes.[27] In general, solvent−molecule interactions lead to shifts in molecular frontier orbital energy levels or electrode Fermi levels,[28,29] which consequently affects molecular charge transport. In the context of redox-active molecules, prior single-molecule electrochemical experiments have shown that nonaqueous ionic liquid solvents yield a larger electrochemical window and a higher reorganization energy compared to aqueous buffers.[30] Despite recent progress, the role of electrolytes and the complex solvent environment on charge transport in redox-active molecules near electrode interfaces is not fully understood.

In this work, we study the charge-transport properties of redox-active viologen-based molecular junctions in the presence of supporting electrolytes with different counterions. A custom electrochemical scanning tunneling microscope-break junction (ECSTM-BJ) instrument is used to directly characterize molecular charge transport at the electrode−electrolyte interface using *in situ* electrochemical gating. Interestingly, our results show that the molecular conductance of viologen-based molecules in the dicationic (2+) state changes by an order of magnitude depending on the anion species (Cl^-, Br^-, I^-, BF_4^-, ClO_4^-, PF_6^-) in the supporting electrolyte. A 10-fold conductance enhancement was also observed in a set of viologen-based junctions upon electrochemical reduction to the radical cationic state. Moreover, molecular junction length was observed to increase upon electrochemical reduction due to reduced electrostatic interactions between the charged viologen core and the electrode surface. Density functional theory (DFT) simulations show that enhanced molecular conductance in different electrolytes arises due to planarization of viologen molecules with corresponding changes in the electronic structures. Broadly, our results highlight the use of single-molecule techniques to understand charge transport at electrode−electrolyte interfaces, including the role of the supporting electrolyte in determining molecular electronic properties.

EXPERIMENTAL AND THEORETICAL METHODS

Synthesis. The synthesis procedures and corresponding chemical characterization information for 1,1′-bis(4-(methylthio)phenyl)-[4,4′-bipyridinine]-1,1′-diium (**DTPV**$^{2+}$), 4,4″-bis(methylthio)-1,1′:4′,1″-terphenyl (**DTP**), 1-methyl-1′-(4-(methylthio)phenyl)-[4,4′-bipyridine]-1,1′-diium (**TPV**$^{2+}$), 1,1′-diphenyl-[4,4′-bipyridine]-1,1′-diium (**DPV**$^{2+}$), and 1-(4-(methylthio)phenyl)-[4,4′-bipyridin]-1-ium (**TPP**$^+$) can be found in the SI.

Bulk Electrochemical Experiments and Ultraviolet−Visible Spectroscopy. Bulk electrochemical experiments were conducted inside an argon-filled glovebox with oxygen and water levels strictly controlled at or below 0.1 ppm. Electrochemical measurements were performed using a potentiostat CHI760E with a 1 mM concentration of five different **DTPV**$^{2+}$ species for cyclic voltammetry and 1 mM concentration of five **DTPV**$^{2+}$ species for bulk electrolysis in 0.1 M $TBAPF_6$ (supporting electrolyte) in propylene carbonate (PC). Voltammetry was carried out using a three-electrode configuration with a 1 mm radius Au-disk macroelectrode, 1.5 mm radius glassy carbon disk macroelectrode, or 12.5 μm radius Pt ultramicroelectrode (UME) as the working electrode, a custom nonaqueous polypyrrole quasi reference electrode (~0.1 M TBAX, where X = PF_6^-, Cl^-, Br^-, BF_4^-, and ClO_4^- in PC), and a Pt wire as the counter electrode. Potential-controlled bulk electrolysis of a stirred solution was carried out in a three-compartment W-cell divided by quartz frits (Adams & Chittenden). A carbon felt working electrode was placed in the middle compartment, and the two lateral compartments contained a Pt mesh counter electrode and the nonaqueous reference electrode described above. For bulk electrolysis of all **DTPV**$^{2+}$ species, the potential was held at −260 mV from $E_{1/2}$, and Pt-UME voltammograms were obtained before and after the electrolysis to confirm complete reduction.

Ultraviolet−visible (UV−vis) absorption spectroscopy was performed to characterize charged and uncharged species. To transfer the charged species from the drybox into the UV−vis spectrophotometer under ambient conditions, a UV−vis cuvette containing charged **DTPV**$^{\bullet+}$ was specially treated to avoid reaction with oxygen that may result in the discharge of **DTPV**$^{\bullet+}$. In particular, under a dry argon atmosphere, a UV−vis cuvette containing 100 μM solution of reduced **DTPV**$^{\bullet+}$ species was tightly wrapped with multiple layers of Teflon tape, followed by two layers of electric tape. The cuvette was further placed into a glass jar, which acted as a temporary mobile argon chamber for transporting the sample through the ambient atmosphere.

Single-Molecule Charge-Transport Measurements. Single-molecule conductance measurements were performed using a custom scanning tunneling microscope-break junction (STM-BJ) setup, as previously described.[31,32] Gold tips were prepared using the 0.25 mm Au wire (99.998%, Alfa Aesar) and coated with Apiezo wax to minimize the diffusion current to below 10 pA in the polar solvent. Gold substrates were prepared by evaporating 10 nm of chromium and 100 nm of gold onto polished AFM metal specimen discs (Ted Pella). Conductance measurements were carried out in deoxygenated propylene carbonate (PC) solutions with 1 mM of the target molecules and 0.1 M corresponding supporting electrolyte. Electrochemical gating ECSTM-BJ experiments were performed under the protection of an Ar atmosphere. The vertical displacement of the gold tip and substrate was controlled by a *z*-axis piezo nanopositioning stage (Madcity labs, mode: Nano-METZ). The translation rate was set to 20 nm/s for all measurements. One- and two-dimensional conductance histograms (5000−10 000 traces for each molecular species) are constructed without any data selection.

Quantum Chemistry Computation. Density functional theory (DFT) calculations were performed to identify the minimum-energy geometry and electronic structure of **DTPV**$^{2+}$. A conformational search was performed for **DTPV**$^{2+}$ in the absence of counterions by enumerating all unique conformational minima associated with the dihedral degrees of freedom of the conjugated rings and performing a geometry optimization for each conformation at the wB97X-D3/def2-TZVPP level of theory using the conductor-like polarizable continuum model (CPCM) with a dielectric constant (ε = 64.9) and a refractive index suitable for the solvent propylene carbonate (PC). All calculations were performed using Orca with default SCF and geometry

https://doi.org/10.1021/acs.jpcc.1c06942
J. Phys. Chem. C 2021, 125, 21862−21872

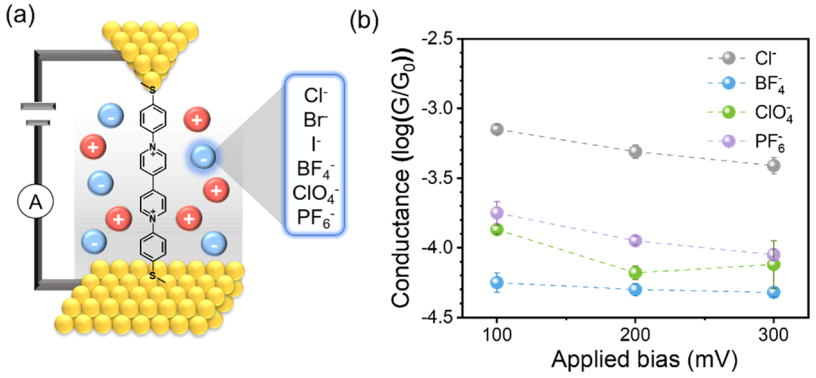

Figure 1. Single-molecule conductance of viologen-based molecules. (a) Schematic of a single **Au-DTPV^{2+}-Au** junction in the electrochemical solution environment containing tetrabutylammonium (TBA) salt as a supporting electrolyte paired with various counterions (**Cl$^-$**, **Br$^-$**, **I$^-$**, **BF$_4^-$**, **ClO$_4^-$**, **PF$_6^-$**) in the scanning tunneling microscope-break junction (STM-BJ) setup. (b) Average molecular conductance of **DTPV^{2+}-Cl$^-$** with TBACl (gray), **DTPV^{2+}-BF$_4^-$** with TBABF$_4$ (blue), **DTPV^{2+}-ClO$_4^-$** with TBAClO$_4$ (green), and **DTPV^{2+}-PF$_6^-$** with TBAPF$_6$ (purple) as a function of applied bias. Error bars represent the standard deviation from three subsamples of each measurement.

optimization convergence criteria. For comparison, a geometry optimization was also performed at the same level of theory (wB97X-D3/def2-TZVPP/CPCM) for the singly reduced state, **DTPV$^+$**, in the absence of counterions. The reduced geometry exhibits considerable planarization of the inter-ring dihedrals and elongation resulting from the increased quinoidal character of the reduced state. Minimum-energy conformers resulting from the ground-state search were then used to seed a conformational search in the presence of two counterions as a function of counterion chemistry. The following procedure was used to identify low-energy geometries for four counterion chemistries used in this study (Cl^-, BF_4^-, ClO_4^-, PF_6^-): pairs of counterions were randomly placed within a 7 Å cubic box surrounding the DTPV^{2+} center of mass, under the constraint that the ions be at least 3 Å apart, for 50 independent iterations. For each placement, a geometry optimization was run at the wB97X-D3/def2-TZVPP/CPCM level of theory. This large basis set, in particular the extra polarization functions, was necessary to accurately describe interactions between the polarizable ions and the hydrogens on the conjugated rings. The resulting minimum-energy geometries were then used as input to wB97X-V/def2-QZVPP/CPCM calculations to obtain the final single-point energies (Supporting Information). To understand the geometries and electronic structure of the reduced states of **DTPV**, two calculations (with one or two counterions adjacent to **DTPV**) were performed to account for the different timescales of electronic reduction. Both sets of calculations were performed at the wB97X-D3/def2-TZVPP/CPCM level of theory (Supporting Information). The resulting torsional angles in **DTPV** are Boltzmann averaged over all distinct conformations found in the conformational search.

Electron-transport calculations were performed using the nonequilibrium Green's function/density functional theory method (NEGF-DFT) via the Atomistix Toolkit package.[32,33] Optimized molecular geometries including the counterions with lowest-energy conformations were used to construct the molecular junctions. The positions for Au atoms and optimized molecules are used for extended junctions. In the transmission calculations, the exchange−correlation potential was approximated by the generalized gradient approximation (GGA) with Perdew−Burke−Ernzerhof (PBE) functional (GGA-PBE).[34] The *k*-point sampling was set to 3 × 3 × 50 (with 50 corresponding to the direction of transport) for all calculations.

RESULTS AND DISCUSSION

Effect of Counterions on Charge Transport in the Dicationic 2+ State. To perform single-molecule charge-transport experiments, we synthesized 1,1′-bis(4-(methylthio)-phenyl)-[4,4′-bipyridinine]-1,1′-diium chloride (**DTPV^{2+}-Cl$^-$**) (Figure 1a), according to the previously reported literature[35] (Supporting Information, Sections S1 and S2, Figures S1−S3). **DTPV^{2+}** contains a redox-active viologen core and two terminal methylthio groups to enable robust contacts with the gold electrode surface.[36] To understand the influence of the electrochemical environment on the charge-transport properties of viologen-based molecules, we compared the molecular conductance of **DTPV^{2+}** in the presence of different supporting electrolytes containing a range of different counterions (Figure 1a). It is known that the supporting electrolytes and counterions of charged redox-active species play a critical role in the physical and electrochemical properties of redox-active systems, such as the viscous flow properties,[37] redox potential,[38,39] and electrochemical reversibility.[40] Prior work has shown that the conductance of a single molecule varies with the concentration of the electroactive salt concentration using copper electrodes.[41] Nevertheless, the role of counterions in organic polar solvents on charge transport in redox-active molecules is not yet fully investigated.

To characterize molecular charge transport in different supporting electrolytes, we used a custom scanning tunneling microscope-break junction (STM-BJ) technique (Figure 1a), as previously reported.[33] For STM-BJ experiments in polar solvents, the gold electrode tip is coated with Apiezon wax to minimize current leakage, as previously described.[42] During measurements, the tip pushes in and out of contact with the substrate electrode to form molecular junctions, and the conductance is measured in units of quantum conductance G_0 ($G_0 = 2e^2/h = 77.5\ \mu S$, where e is the electron charge and h is Planck's constant). In the absence of a molecular junction, the conductance drops sharply to the noise floor as the tip moves away from the substrate. In the presence of a molecular junction, a conductance plateau is observed below G_0 as the tip moves away from the substrate before the molecular junction ruptures. Logarithm-binned one-dimensional conductance histograms are constructed by compiling 5000−10 000 traces from individual experiments and analyzed to determine the most probable molecular conductance.[43]

https://doi.org/10.1021/acs.jpcc.1c06942
J. Phys. Chem. C 2021, 125, 21862−21872

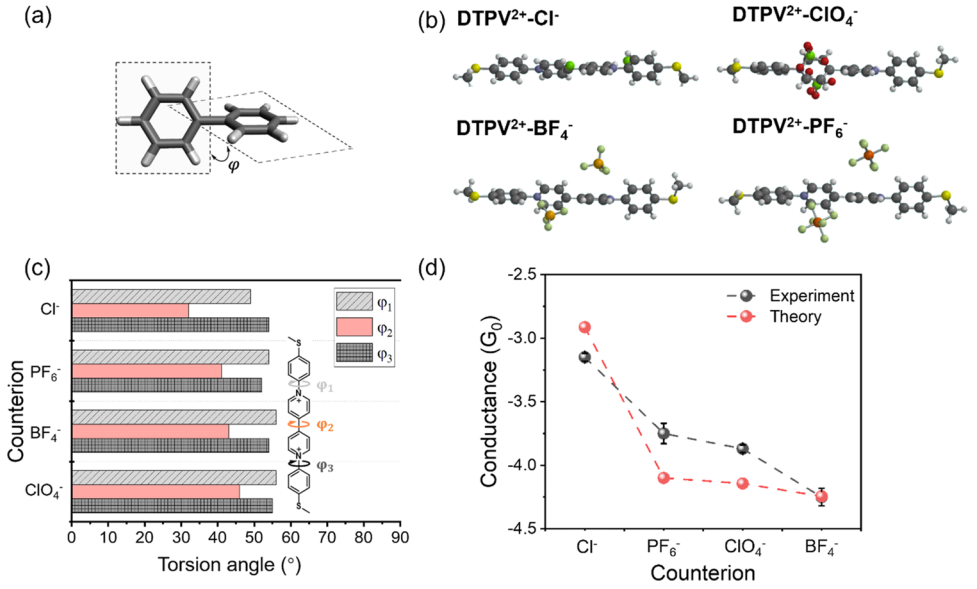

Figure 2. DFT simulations of molecular conformation showing counterion effects on conductance. (a) Torsional angles φ between the pyridinium−pyridinium rings and phenyl−pyridinium rings depend on the surrounding counterions. (b) DFT-optimized minimum-energy molecular geometries of **DTPV^{2+}** paired with different counterions (Cl^-, BF_4^-, ClO_4^-, PF_6^-). (c) Average torsional angles of **DTPV^{2+}-X** induced by different counterions (Cl^-, BF_4^-, ClO_4^-, PF_6^-) from DFT simulations. (d) Comparison of the experimental molecular conductance from STM-BJ measurement at 100 mV applied bias (gray) and the zero-bias transmission from NEGF-DFT calculations (red) for **DTPV^{2+}** paired with Cl^-, BF_4^-, ClO_4^-, and PF_6^-. Error bars represent the standard deviation from three subsamples of each measurement.

We began by studying the molecular conductance of a series of six different solutions of 1 mM **DTPV^{2+}** in propylene carbonate paired with different anions prepared by ion exchange, including tetrafluoroborate (**BF_4^-**), perchlorate (**ClO_4^-**), hexafluorophosphate (**PF_6^-**), bromide (**Br^-**), and iodide (**I^-**), in addition to the synthesized chloride (**Cl^-**) species (Figure S4). We determined the molecular conductance for each system in the presence of 0.1 M tetrabutylammonium salts with corresponding counterions as the supporting electrolyte using a tip−substrate voltage V_b of 100, 200, and 300 mV. The supporting electrolytes used in this work have similar ion-pair dissociation constants and conductivities in propylene carbonate.[44,45] Initial experiments were performed using the standard STM-BJ method without implementing a gate electrode (*vide infra*), such that viologen molecules remain in the dicationic (2+) state (Supporting Information, Section S3). Interestingly, our results show that the average molecular conductance is significantly affected by the counterion species in the environment (Figure 1b). Compared to **BF_4^-**, the molecular conductance of **DTPV^{2+}** is enhanced by one order of magnitude in the presence of **Cl^-** anions. In general, the molecular conductance follows an overall increasing order with the counterion of **BF_4^-** < **ClO_4^-** < **PF_6^-** < **Cl^-** over the range of applied bias V_b. Control molecules **TPV^{2+}** and **DPV^{2+}** containing only one or no methylthiol anchors were also synthesized and characterized using STM-BJ (Figure S5). The results from 2D conductance histograms show that the control molecules **TPV^{2+}** and **DPV^{2+}** are unable to form robust junctions with conductance and junction lengths comparable to **DTPV^{2+}**, which strongly supports the observation that the conductance signal in **DTPV^{2+}** does not arise from molecular junctions formed by contacts between the viologen (bipyridinium) core and gold electrodes. In contrast to the prior work where the bipyridinium moiety was reported to serve as an anchor group,[46,47] the addition of the supporting electrolyte weakens electrostatic interactions between the viologen moiety and gold electrodes, thereby preventing the viologen moiety to serve as the anchor group.

We further studied the molecular displacements during single-molecule conductance experiments. Interestingly, 2D conductance histograms show that junctions formed by **DTPV^{2+}-Br^-** and **DTPV^{2+}-I^-** exhibit relatively short displacements compared to the other four counterion systems in the entire tested bias range (Figure S6). Prior work on anion adsorption has shown that weakly solvated halide ions form chemical bonds with metal surfaces following the order **I^-** > **Br^-** > **Cl^-**.[48−50] Chemisorption at charged electrode surfaces may block active sites or change the binding energy[S1] for the anchor groups to interact with gold electrodes, which results in weakly bound molecular junctions with **Br^-** or **I^-** passivated surfaces in our system. Similar undesirable anion adsorption was also observed for the control molecule **DTP**, where the charged viologen moiety is replaced by neutral phenyl rings (Figures S7 and S8). Our results suggest that **Br^-** and **I^-** ions prevent **DTP** from forming robust molecular junctions and therefore exhibit shorter junction displacements compared to **Cl^-**, **BF_4^-**, **ClO_4^-**, and **PF_6^-**. Nevertheless, prior work reported that the adsorption strengths and surface coverages of **Cl^-**, **BF_4^-**, **ClO_4^-**, and **PF_6^-** were substantially lower than **Br^-** and **I^-**.[52,53] In general, these results are consistent with our observations that **Cl^-**, **BF_4^-**, **ClO_4^-**, and **PF_6^-** do not significantly inhibit molecular junction formation between the tip and substrate electrodes. Based on these results, **DTPV^{2+}** paired with **Br^-** and **I^-** was not considered for subsequent analyses.

To understand the role of counterions in molecular conductance, we performed DFT simulations of **DTPV^{2+}** with different counterion species in the system (Supporting Information, Section S4). **DTPV^{2+}** consists of two pyridinium rings with a phenyl group on each terminus connected by a C−C single bond, which allows for substantial conformational

https://doi.org/10.1021/acs.jpcc.1c06942
J. Phys. Chem. C 2021, 125, 21862−21872

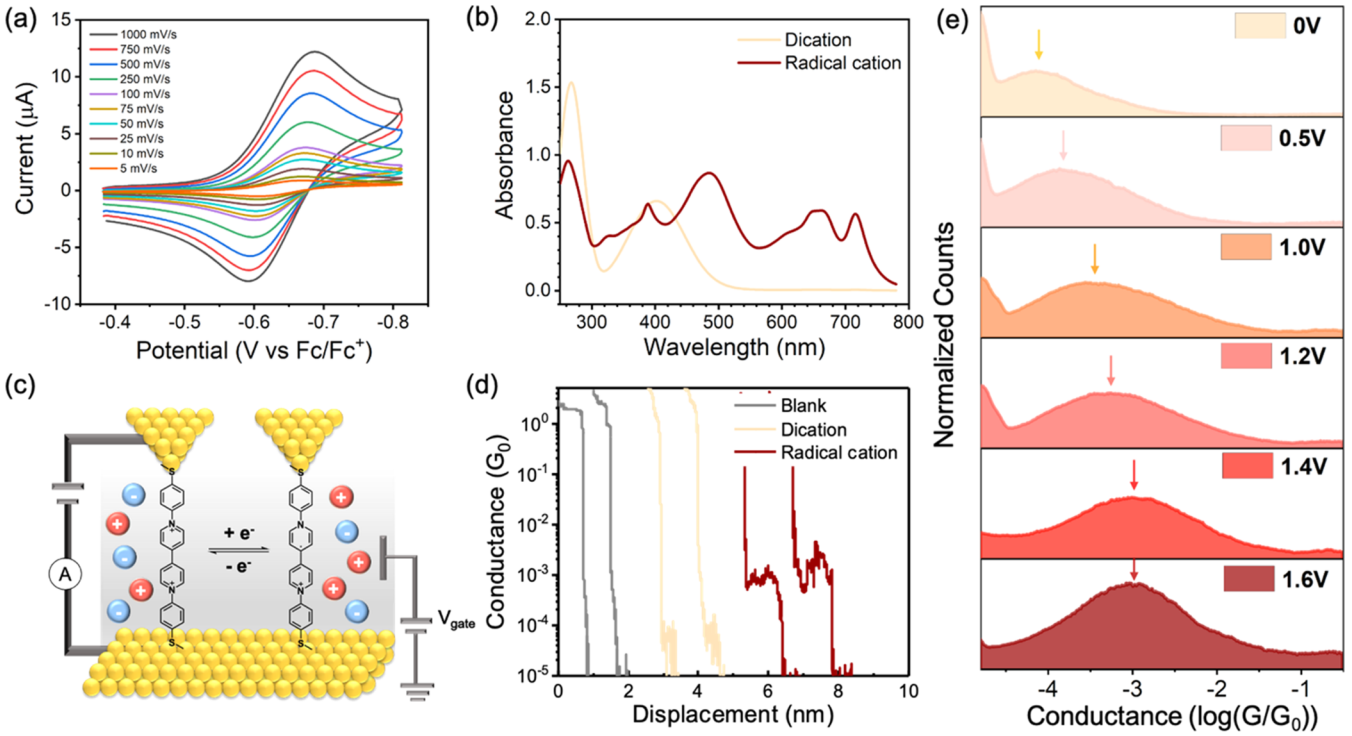

Figure 3. Bulk electrochemical and single-molecule electrochemical experiments on **DTPV^{2+}-PF$_6^-$**. (a) Cyclic voltammogram of 1.35 mM **DTPV^{2+}-PF$_6^-$** in propylene carbonate with 0.1 M $TBAPF_6$ as the supporting electrolyte at scan rates ranging from 5 to 1000 mV/s on a Au-disk macroelectrode (1 mm radius) under an argon atmosphere. (b) UV−vis absorption spectra of **DTPV^{2+}** in the dicationic state (yellow) and the radical cationic state (red). (c) Schematic of the electrochemical scanning tunneling microscope-break junction (ECSTM-BJ) instrument. Single **Au-DTPV^{2+}-Au** junctions undergo reversible redox switching via electrochemical gating in the presence of the supporting electrolyte (tetrabutylammonium salt). (d) Characteristic single-molecule conductance traces of a blank solution (black), **DTPV^{2+}-PF$_6^-$** in the dicationic state (yellow) at a gate voltage V_g = 0 V, which is well below the oxidation/reduction threshold, and **DTPV$^{+\cdot}$-PF$_6^-$** in the radical cationic state (red) at V_g = 1.6 V, which is well above the oxidation/reduction threshold. (e) Logarithm-binned 1D conductance histograms for 1 mM **DTPV^{2+}-PF$_6^-$** in a solution of PC with 0.1 M tetrabutylammonium hexafluorophosphate ($TBAPF_6$) at V_g = 0, 0.5, 0.8, 1, 1.2, 1.4, and 1.6 V.

variation by rotation about the torsional angles between the phenyl−pyridinium ring and the bipyridinium rings (Figure 2a). Prior work reported that intramolecular charge transport decreases with an increased interplane torsional angle in biphenyl systems,[54−56] which suggests that similar effects may arise in **DTPV^{2+}** as a function of the solution environment. Therefore, DFT calculations were used to identify the minimum-energy geometry of **DTPV^{2+}** in the presence of two counterions as a function of counterion chemistry (Tables S1−S4). Geometry optimization was performed using the wB97X-D3/def2-TZVPP with a conductor-like polarizable continuum model (CPCM) in ORCA;[57] this level of theory provides a large basis set, polarization functions, and a solvent model to accurately describe interactions between the polarizable ions and hydrogen atoms on the conjugated rings.

The results from molecular modeling show that counterions play a key role in molecular conformations (Figure 2b,c). In particular, the DFT results reveal that the average torsional angles between the two pyridinium planes (i.e., φ_2) are significantly influenced by the counterion species. For all counterion species, the interactions between the polarizable negative ions and the positively charged pendant sp^2 hydrogens on the conjugated rings play a critical role in the stabilization of observed molecular geometries, even those that are nonplanar. Low-energy conformations of **DTPV^{2+}-Cl$^-$** exhibit minimal interaction between **Cl$^-$** and the polarizable π electron system, with the ion instead preferring to associate with positively charged sp^2 hydrogens on neighboring conjugated rings, inducing planarity (Table S1). This effect is attributed to the small size and large charge density of **Cl$^-$** such that association with the backbone provides minimal energetic benefit, and **Cl$^-$** prefers interacting solely with the sp^2 hydrogens. As the size of the counterions increases (e.g., for larger counterions **BF$_4^-$**, **ClO$_4^-$**), the coulombic charge density of the counterion decreases, thereby penalizing conformations in which the ions associate solely with sp^2 hydrogens, and the **DTPV^{2+}**-counterion system lowers its energy by associating with the polarizable π-electron system of the backbone. Concomitant with counterion association with the π system is the geometric distortion of the backbone and the twisting of the dihedral angles to accommodate the presence of the counterion, with the twisting primarily resulting from the need to reorient sp^2 hydrogens to maximize electrostatic interactions with the associated ions. Overall, **Cl$^-$** induces a low-energy molecular geometry that results in the most planar backbone structure, which is counterintuitively followed by **PF$_6^-$**. For the case of **PF$_6^-$**, the counterion size is large enough that it cannot easily fit within the same distorted pockets created for **BF$_4^-$** and **ClO$_4^-$**, leading to association further away from the backbone and reduced geometric distortion. In general, intermediate-sized anions **ClO$_4^-$** and **BF$_4^-$** result in the most geometrically distorted structures between the two pyridinium planes.

We next modeled molecular junctions containing **DTPV^{2+}-Cl$^-$**, **DTPV^{2+}-BF$_4^-$**, **DTPV^{2+}-ClO$_4^-$**, and **DTPV^{2+}-PF$_6^-$** using their corresponding optimized geometries and performed

https://doi.org/10.1021/acs.jpcc.1c06942
J. Phys. Chem. C 2021, 125, 21862−21872

conductance calculations with nonequilibrium Green's function-density functional theory (NEGF-DFT) simulations via the Atomistix Toolkit package (Figure S9).[32] Figure 2d shows a comparison between the calculated transmission functions at zero bias from NEGF-DFT calculations and the experimental conductance values from STM-BJ measurements. The results from NEGF-DFT simulations are qualitatively consistent with the overall trend in an increasing order of **DTPV^{2+}-BF$_4^-$** < **DTPV^{2+}-ClO$_4^-$** < **DTPV^{2+}-PF$_6^-$** < **DTPV^{2+}-Cl$^-$**. The most planar structure of **DTPV^{2+}-Cl$^-$** has closely aligned molecular frontier energy levels with the electrode Fermi leads, which leads to a strongly enhanced conductance value around 10^{-3} G_0, which is approximately 20 times larger than **DTPV^{2+}-BF$_4^-$** at 5.7×10^{-5} G_0. Taken together, these results suggest that molecular conformation and differences in anion adsorption lead to the conductance variations observed in the STM-BJ experiments.

Bulk-Scale Electrochemical Characterization of Redox-Active Species. Viologen molecules are capable of storing two electrons and therefore undergo two reduction steps in different electrochemical environments. Transitioning between different redox states induces changes in molecular conformation or electronic structure that may result in changes in charge-transport behavior.[58,59] It is therefore essential to understand charge transport in different redox states and in the presence of different counterions. To this end, we characterized the electrochemical and optical properties of **DTPV^{2+}** in different counterion environments of **Cl$^-$**, **BF$_4^-$**, **ClO$_4^-$**, and **PF$_6^-$** using cyclic voltammetry (CV) and UV−vis spectroscopy before and after bulk electrolysis (Figures S10 and S11). Figure 3a shows the scan rate dependence for a 1.35 mM solution of **DTPV^{2+}-PF$_6^-$** with 0.1 M TBAPF$_6$ in propylene carbonate on a Au-disk macroelectrode (area A = 0.03 cm^2) under an argon atmosphere. The same scan rate dependence was carried out on a glassy carbon electrode, and no difference was observed in the electrochemical behavior (Figure S11). The electrochemical response of **DTPV^{2+}-PF$_6^-$** demonstrates a reversible reduction of the dication to a radical cation centered at −0.64 V versus Fc/Fc$^+$. Scan rate-dependent CV experiments show linearity of the peak current versus the square root of the scan rate (Figure S12), indicating diffusional control of **DTPV^{2+}-PF$_6^-$** reactivity at the electrode. Randles−Sevcik analysis reveals a diffusion coefficient for **DTPV^{2+}-PF$_6^-$** of 1.20 ± 0.01 × 10^{-10} m^2/s. Scan rate-dependent voltammetry for **Cl$^-$**, **BF$_4^-$**, and **ClO$_4^-$** counterions is also shown in Figures S10 and S11. The electrochemical response of all **DTPV^{2+}-X$^-$** species demonstrates a reversible reduction of the dication to a radical cation centered at the following potentials on a Au-disk electrode: $E_{1/2}$ (**DTPV^{2+}-Cl$^-$**) = −0.66 V; $E_{1/2}$ (**DTPV^{2+}-BF$_4^-$**) = −0.64 V; and $E_{1/2}$ (**DTPV^{2+}-ClO$_4^-$**) = −0.64 V versus Fc/Fc$^+$ on the Au disk. The PF$_6^-$ and ClO$_4^-$ species show similar CV responses, with comparable diffusion coefficients according to the Randles−Sevcik analysis. However, the Cl$^-$ and BF$_4^-$ species exhibited lower peak currents in CV experiments due to lower solubility in propylene carbonate.

UV−vis spectroscopy was used to characterize the optical properties of the initial and bulk electrolyzed reduced species (Figure 3b). Here, a 1.35 mM solution of **DTPV^{2+}-PF$_6^-$** was electrolyzed at an overpotential of −0.8 V versus Fc/Fc$^+$ to a state of charge of 1.0, where the charging current dropped to <1% of the initial current. A change in color from a clear orange to dark green suspension was observed as the solution was charging. The single charging cycle resulted in a coulombic efficiency of 98%. To assess the extent of **DTPV^{2+}-PF$_6^-$** charging in solution, cyclic voltammograms using a platinum ultramicroelectrode (UME) were obtained prior to charging and immediately following the charging process (Figure S12). UME voltammetric waves for both uncharged and charged species exhibit a sigmoidal shape and generally achieve a steady-state current. UV−vis measurements show the shift of the **DTPV^{2+}-PF$_6^-$** 400 nm absorption peak that is specific to viologen-type compounds compared to the 484 nm peak of the singly reduced radical cation (Figure 3b).[60,61] The presence of peaks in the 600−800 nm region confirms the formation of charge-transfer complexes. Moreover, similar shifts in UV−vis adsorption spectra are observed in **DTPV^{2+}** paired with different counterions (Figure S10).

Molecular Charge Transport with Electrochemical Gating. To further understand molecular charge transport in complex electrochemical environments, we used a custom electrochemical scanning tunneling microscope-break junction (ECSTM-BJ) instrument (Figure 3c), which consists of two working electrodes to form molecular junctions and a third gate electrode to modulate the electrochemical environment. In brief, our standard STM-BJ instrument[62,63] was modified by inserting a platinum electrode into the fluid cell to serve as a gate electrode, which can be used to switch between different molecular redox states by applying an electrochemical gate potential. In addition to the applied tip-to-substrate voltage V_b, a gate potential V_g is separately applied relative to the substrate electrode using a gate electrode, as previously described.[64,65]

To investigate charge transport in **DTPV^{2+}** in the reduced state, we characterized molecular conductance in different electrolyte systems using ECSTM-BJ by controlling the gate potential V_g in a Ar-purged box (Figure 3c). Prior to performing experiments on **DTPV^{2+}**, *in situ* linear sweep voltammetry (LSV) was performed in the ECSTM setup to determine the oxidation potential of a solution containing ∼1 mM ferrocene and 0.1 M TBAPF$_6$ (Figure S13). As discussed in the prior work,[64] the sign of the electrochemical potential at which the redox reactions occur in the ECSTM setups is generally opposite to the conventional voltammogram measurement, where the potential is applied on the working electrode relative to the reference electrode. Therefore, in our ECSTM setup (Figure S13), the oxidation of ferrocene occurs at a negative gate potential (V_g < 0), whereas the reduction of **DTPV^{2+}** occurs at a positive gate potential.

In ECSTM-BJ experiments, the gate potential V_g was varied in each set of measurements while maintaining a constant applied bias V_b at 100 mV between the tip and the substrate. Considering the behavior of **DTPV^{2+}-PF$_6^-$**, our results show that the average molecular conductance gradually increases as the gate potential V_g is increased within the electrochemical window of the first reduction from **DTPV^{2+}-PF$_6^-$** to **DTPV^{+}-PF$_6^-$** (Figures 3e and S13). Around a gate potential of 1.4 V where **DTPV^{2+}-PF$_6^-$** is fully reduced to **DTPV^{+}-PF$_6^-$**, the molecular conductance reaches a plateau at around 1×10^{-3} G_0, which is more than 10-fold larger than the conductance value at 0 V gate potential (7.1×10^{-5} G_0). In addition, the peak height of the 1D conductance histograms significantly increases with significantly more data points in the conductance plateau at the reduced state due to the enhanced stretching of molecular junctions (Figures 3e and S14), as highlighted in the characteristic single-molecule conductance traces (Figure 3d) and discussed below.

https://doi.org/10.1021/acs.jpcc.1c06942
J. Phys. Chem. C 2021, 125, 21862−21872

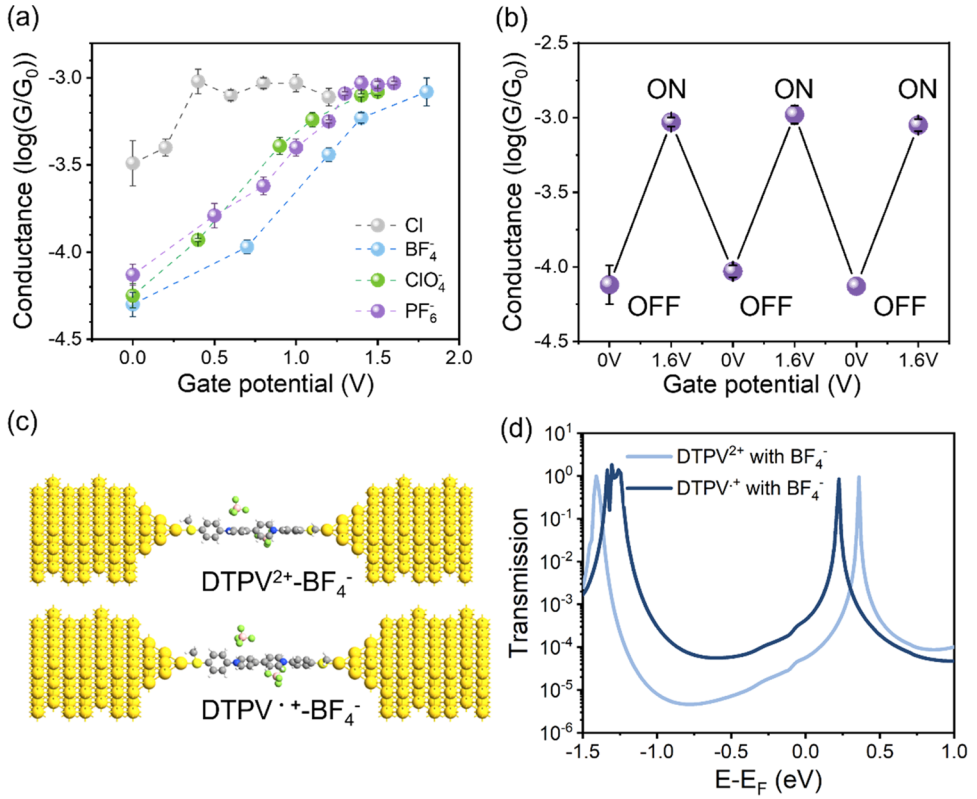

Figure 4. Electrochemical single-molecule charge-transport experiments on viologen-based molecules with different counterions. (a) Peak conductance values of **DTPV^{2+}-Cl$^-$** (gray), **DTPV^{2+}-BF$_4^-$** (blue), **DTPV^{2+}-ClO$_4^-$** (green), and **DTPV^{2+}-PF$_6^-$** (purple) versus the gate potential V_g with a constant applied bias at 100 mV. (b) Reversible ON−OFF conductance switch of **DTPV^{2+}-PF$_6^-$** between V_g = 0 and 1.6 V for three cycles. Error bars represent the standard deviation from three subsamples of each measurement. (c) Configurations **Au-(DTPV^{2+}-BF$_4^-$)-Au** junction (top) and **Au-(DTPV^{2+}-BF$_4^-$)^{plan}-Au** junction (bottom) with the planarized conformation adopted from the optimized geometry of the radical cationic state. (d) Transmission spectra as a function of energy for the twisted **Au-(DTPV^{2+}-BF$_4^-$)-Au** with the geometry of the 2+ state (light blue) and **Au-(DTPV^{2+}-BF$_4^-$)^{plan}-Au** junction with the planarized conformation adopted from the optimized geometry of the radical cationic state (dark blue). E_F is the Fermi level of the junction.

We next repeated the conductance measurements using the ECSTM-BJ setup on **DTPV^{2+}** molecules with different counterions (Figure 4). Each system shows a conductance increase from a low conductance region (~3 × 10^{-4} G_0 for **DTPV^{2+}-Cl$^-$** and <1 × 10^{-4} G_0 for **DTPV^{2+}-ClO$_4^-$** and **DTPV^{2+}-BF$_4^-$**) to a high conductance region around 1 × 10^{-3} G_0 upon being electrochemically reduced by the gate potential (Figures 4a and S14). The conductance switch between **DTPV^{2+}** and **DTPV$^{\cdot+}$** was reversible as shown with the counterion of **PF$_6^-$** by repeating the measurements on the same sample with gate potential V_g cycled between 0 and 1.6 V (Figure 4b). The conductance peak values yielded an average on/off ratio of ~10 for at least 3 cycles. Prior work[65] reported that the conductance of molecules with the lowest unoccupied molecular orbital (LUMO) dominant pathways generally increases with increasing positive gate potential. Therefore, the observed conductance modulation suggests that molecular charge transport in our viologen molecules is LUMO-dominated, which is consistent with prior reports on pyridinium or bipyridinium molecules.[35,66] Overall, the conductance modulation pattern is consistent with charge transport occurring by a direct tunneling (superexchange) mechanism instead of a two-step Kuznetsov−Ulstrup hopping or a resonant tunneling model, which would otherwise exhibit a bell-shaped conductance response near the redox potential.[18,67]

Similar patterns of molecular conductance in electrochemically gated environments have been observed in prior studies on flexible alkyl-chain-terminated ferrocene[23] and viologen,[17] norcorrole-based Ni(II) complexes,[68] and polyoxometalates.[69] Nevertheless, our results in Figure 4a show a more gradual increase in molecular conductance with V_g compared to prior work, which suggests that the electrostatics of the diffuse layer plays a role in modulating charge transport. Indeed, it has been shown that the molecular frontier orbital energy levels in redox-inactive molecules can be electrostatically shifted relative to the electrode Fermi level.[70] However, such electrostatic shifts generally result in relatively small changes in conductance over the range of V_g applied in this work. To estimate the contribution of the electrostatics in the diffuse layer to the charge-transport properties, we tested a similar LUMO-conducting molecule **TPP** that contains only one pyridinium group but does not undergo a redox reaction within the electrochemical potential window studied here (Figure S15). Indeed, **TPP** only showed a 3-fold increase in conductance between V_g = 0 and 1.5 V, which is significantly smaller than the conductance change observed for **DTPV^{2+}** over a similar range of V_g. Overall, these results suggest that the electrostatics of the diffuse layer plays a relatively minor role in the charge-transport behavior of the reduced species.

To further understand the increase in molecular conductance in the reduced state, we performed geometry optimization with the molecules in the radical cationic state.

https://doi.org/10.1021/acs.jpcc.1c06942
J. Phys. Chem. C 2021, 125, 21862−21872

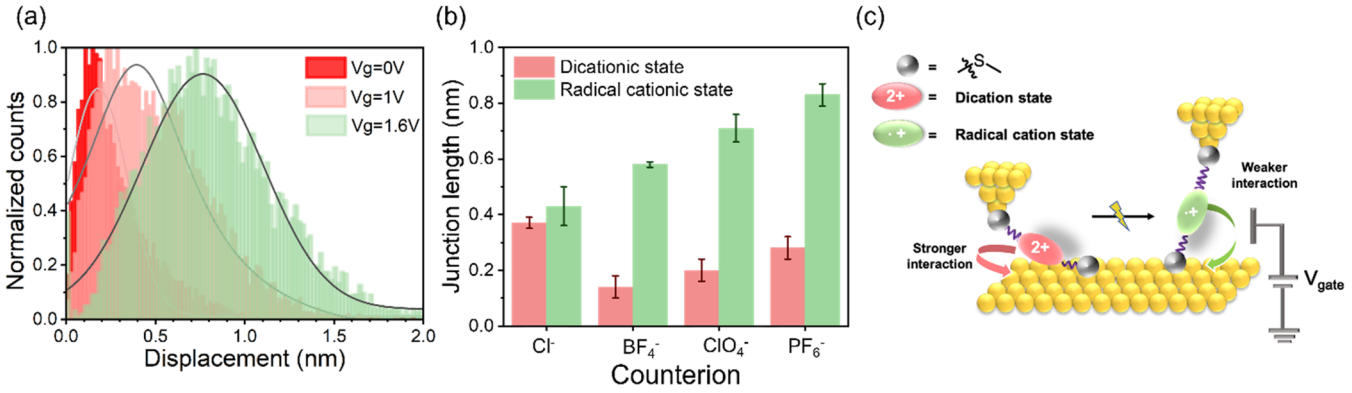

Figure 5. Molecular junction displacement of viologen-based molecules. (a) Logarithm-binned 1D displacement histograms of **DTPV^{2+}-PF$_6^-$** with 0.1 M TBAPF4 in PC at V_g = 0 (red), 1 (pink), and 1.6 V (green). (b) Average molecular junction lengths with different supporting electrolyte counterions for **DTPV^{2+}** in the dicationic state (pink) and the radical cationic state (green). Error bars represent the standard deviation from three subsamples of each measurement. (c) Schematic of molecular extension showing changes in the strength of viologen adsorption at the electrode surface as the molecule is electrochemically reduced from the dicationic state to the radical cation state.

Over the timescale of electrochemical reduction, the two associated counterions are expected to remain in the vicinity of the molecular junction. Therefore, we modeled molecular geometries by placing two anions in the junction. DFT simulations show a change in the electronic band structure of the molecule in the radical cationic state. The position of the transport band in the radical cationic state shifts significantly compared to that in the dicationic 2+ state, which partially explains the enhanced charge transport in the reduced state. Compared with the frontier molecular orbital energy levels of the 2+ state, the SOMO energy levels of the radical cationic state for all four counterions are around −6 eV (Table S6) and therefore more closely aligned with the electrode Fermi level (E_F = −5.1 eV for gold). However, the shift of the energy bands is not the only reason for the enhanced conductance in the reduced state. We observed that the torsional angles of the two pyridinium rings strongly planarize for all four counterions (Figure S16 and Tables S5 and S6). These results are consistent with prior work reporting a reduction in torsion angles between two pyridinium planes in the solid-state structures of diphenylviologen[71] and macrocyclic viologen.[72]

We next performed NEGF-DFT simulations to determine the transmission of **DTPV^{+}** in the presence of counterions (Figure 4c). Transport in the radical cationic electronic state is approximated via a calculation of transport in the dicationic electronic state using the optimized radical cationic state geometry. The transmission of the planarized junction is denoted by **Au-(DTPV^{2+}-BF$_4^-$)^{plan}-Au** and is compared with that of the twisted geometry **Au-(DTPV^{2+}-BF$_4^-$)-Au** at the 2+ state (Figure 4d). The planarization of bipyridinium rings leads to a conductance enhancement of approximately 8-fold in the reduced state due to a smaller tunneling barrier. However, at long timescales, the equilibrium state of the reduced molecule likely only consists of a single nearby counterion provided to enforce charge neutralization. Indeed, in all cases, substantial planarization was observed with one counterion in the reduced state relative to the ground state with enhanced transmission (Table S6). Overall, the DFT simulations accurately explain the trends of increasing conductance of the reduced radical cationic state compared to the dicationic state with different counterion species, mainly as a result of molecular planarization and concomitant changes in the electronic state (Figures S17−S20).

To understand the mechanical stability of molecular junctions in complex electrochemical environments, we constructed 1D displacement histograms, as described in prior work (Figures S21 and S22).[31] 1D displacement histograms are fit with a Gaussian distribution to obtain the average tip-to-substrate displacement, which represents how the molecular junction lengths change as a function of the gate potential and counterion environment. The onset of junction displacement is defined as the point of metal nanowire rupture between the tip and substrate electrode.[31] Our results show that molecular junctions in the presence of **PF$_6^-$** are extended to a maximum displacement of ∼0.28 nm at a gate potential of 0 V (Figure 5a). Remarkably, when the molecules are reduced to the radical cationic state at the gate potential at 1.6 V, molecular junction displacement reaches a length of ∼0.83 nm. We further compared the molecular displacements in the dicationic state at V_g = 0 V and the radical cationic state at an overpotential ($\eta = |V_g - E_{p/2}|$) of 0.4 V (Figure S13) across the molecular junctions in all four counterion environments (Figure 5b). In these conditions, the radical cationic state of the molecular junctions is extended to distances longer than the dicationic state. We excluded the possibility that the increased junction length results from stacked viologen radical dimers because **DTPV^{2+}** generally does not form stable dimer junctions in these conditions, as evidenced by gate voltage-dependent conductance measurements of a control molecule **TPV^{2+}** containing only one anchor group. Overall, our results show that when **TPV^{2+}** is reduced by electrochemical gating, there is no evidence of stable dimer junction formation (Figure S23).

Based on these results, we propose that electrostatic interactions mediate the molecular stretching process of viologens between the tip and electrode surface (Figure 5c).[46,47,73,74] Upon reducing viologens from the dicationic to the radical cationic state, interactions between the positively charged molecular backbone and the electrode surface are weakened, thereby enabling molecular junctions to become more extended. On the other hand, the control molecule **DTP** lacking a charged moiety (Figure S24) exhibits no changes in displacement across different gate potentials due to the absence of electrostatic interactions with the substrate. However, it is possible that additional complex molecular geometry changes are associated with the reduced state of the

https://doi.org/10.1021/acs.jpcc.1c06942
J. Phys. Chem. C 2021, 125, 21862−21872

molecule. DFT simulations indicate a slight increase (<0.5 Å) in the molecular size of **DTPV** in the reduced state due to the flattening of dihedral angles and the presence of a quinoidal structure that extends the double bonds in the system (Supporting Information, Section S7). On the other hand, **DTP** contains an uncharged redox-inactive core that does not undergo conformational or electronic structural changes. Overall, our results suggest that changes in molecular junction lengths arise due to electrostatic interactions and molecular geometry elongation.

CONCLUSIONS

In this work, we systematically study charge transport in viologen-containing molecules near electrode interfaces using a combination of single-molecule experiments, bulk electrochemical experiments, and molecular modeling. Our work reveals a reversible 10-fold change in the conductance of viologen molecules in electrolyte solutions using *in situ* electrochemical gating. Moreover, our results reveal a surprising dependence of the charge-transport properties of viologen molecules on the counterion environment. DFT simulations reveal that molecular planarization and better energy alignment lead to enhancement of charge transport upon electrochemical reduction. In addition, different counterion environments induce conformational twisting between the two planes of the viologen cores to different extents, which results in differences in molecular conductance. Overall, this work advances our understanding of charge transport in redox-active molecules in complex electrochemical environments.

ASSOCIATED CONTENT

Supporting Information

The Supporting Information is available free of charge at https://pubs.acs.org/doi/10.1021/acs.jpcc.1c06942.

Details of molecular synthesis and chemical characterization; NMR characterization of synthesized molecules; supporting figures for STM-BJ and electrochemical ECSTM-BJ experiments; molecular modeling of viologens in dicationic and reduced states; bulk electrochemical and UV−vis characterization of viologens; molecular junction stability analysis (PDF)

AUTHOR INFORMATION

Corresponding Author

Charles M. Schroeder − *Department of Chemical and Biomolecular Engineering, University of Illinois at Urbana-Champaign, Urbana, Illinois 61801, United States; Department of Chemistry, Department of Materials Science and Engineering, and Beckman Institute for Advanced Science and Technology, University of Illinois at Urbana-Champaign, Urbana, Illinois 61801, United States; Joint Center for Energy Storage Research (JCESR), Argonne, Illinois 60439, United States;* orcid.org/0000-0001-6023-2274; Email: cms@illinois.edu

Authors

Jialing Li − *Department of Chemical and Biomolecular Engineering, University of Illinois at Urbana-Champaign, Urbana, Illinois 61801, United States; Beckman Institute for Advanced Science and Technology, University of Illinois at Urbana-Champaign, Urbana, Illinois 61801, United States; Joint Center for Energy Storage Research (JCESR), Argonne, Illinois 60439, United States*

Sanja Pudar − *Department of Chemistry, University of Illinois at Urbana-Champaign, Urbana, Illinois 61801, United States; Joint Center for Energy Storage Research (JCESR), Argonne, Illinois 60439, United States*

Hao Yu − *Department of Chemical and Biomolecular Engineering, University of Illinois at Urbana-Champaign, Urbana, Illinois 61801, United States; Joint Center for Energy Storage Research (JCESR), Argonne, Illinois 60439, United States;* orcid.org/0000-0002-1594-769X

Songsong Li − *Department of Materials Science and Engineering and Beckman Institute for Advanced Science and Technology, University of Illinois at Urbana-Champaign, Urbana, Illinois 61801, United States; Joint Center for Energy Storage Research (JCESR), Argonne, Illinois 60439, United States*

Jeffrey S. Moore − *Department of Chemistry, Department of Materials Science and Engineering, and Beckman Institute for Advanced Science and Technology, University of Illinois at Urbana-Champaign, Urbana, Illinois 61801, United States; Joint Center for Energy Storage Research (JCESR), Argonne, Illinois 60439, United States;* orcid.org/0000-0001-5841-6269

Joaquín Rodríguez-López − *Department of Chemistry and Beckman Institute for Advanced Science and Technology, University of Illinois at Urbana-Champaign, Urbana, Illinois 61801, United States; Joint Center for Energy Storage Research (JCESR), Argonne, Illinois 60439, United States;* orcid.org/0000-0003-4346-4668

Nicholas E. Jackson − *Department of Chemistry, University of Illinois at Urbana-Champaign, Urbana, Illinois 61801, United States;* orcid.org/0000-0002-1470-1903

Complete contact information is available at: https://pubs.acs.org/10.1021/acs.jpcc.1c06942

Notes

The authors declare no competing financial interest.

ACKNOWLEDGMENTS

The research was financially supported by the Joint Center for Energy Storage Research (JCESR), an Energy Innovation Hub funded by the U.S. Department of Energy, Office of Science, Basic Energy Sciences.

REFERENCES

(1) Li, M.; Rhodes, Z.; Cabrera-Pardo, J. R.; Minteer, S. D. Recent Advancements in Rational Design of Non-Aqueous Organic Redox Flow Batteries. *Sustainable Energy Fuels* **2020**, *4*, 4370−4389.

(2) Hromadová, M.; Vavrek, F. Electrochemical Electron Transfer and Its Relation to Charge Transport in Single Molecule Junctions. *Curr. Opin. Electrochem.* **2020**, *19*, 63−70.

(3) Bello, L.; Sing, C. E. Mechanisms of Diffusive Charge Transport in Redox-Active Polymer Solutions. *Macromolecules* **2020**, *53*, 7658−7671.

(4) Sato, K.; Ichinoi, R.; Mizukami, R.; Serikawa, T.; Sasaki, Y.; Lutkenhaus, J.; Nishide, H.; Oyaizu, K. Diffusion-Cooperative Model for Charge Transport by Redox-Active Nonconjugated Polymers. *J. Am. Chem. Soc.* **2018**, *140*, 1049−1056.

(5) Albrecht, T. Electrochemical Tunnelling Sensors and Their Potential Applications. *Nat. Commun.* **2012**, *3*, No. 829.

(6) Burgess, M.; Hernandez-Burgos, K.; Schuh, J. K.; Davila, J.; Montoto, E. C.; Ewoldt, R. H.; Rodriguez-Lopez, J. Modulation of the

Electrochemical Reactivity of Solubilized Redox Active Polymers Via Polyelectrolyte Dynamics. *J. Am. Chem. Soc.* **2018**, *140*, 2093−2104.
(7) Rhodes, Z.; Cabrera-Pardo, J. R.; Li, M.; Minteer, S. D. Electrochemical Advances in Non-Aqueous Redox Flow Batteries. *Isr. J. Chem.* **2021**, *61*, 101−112.
(8) Montoto, E. C.; Cao, Y.; Hernández-Burgos, K.; Sevov, C. S.; Braten, M. N.; Helms, B. A.; Moore, J. S.; Rodríguez-López, J. Effect of the Backbone Tether on the Electrochemical Properties of Soluble Cyclopropenium Redox-Active Polymers. *Macromolecules* **2018**, *51*, 3539−3546.
(9) Seguin, T. J.; Hahn, N. T.; Zavadil, K. R.; Persson, K. A. Elucidating Non-Aqueous Solvent Stability and Associated Decomposition Mechanisms for Mg Energy Storage Applications from First-Principles. *Front. Chem.* **2019**, *7*, No. 175.
(10) Zhao, Y.; Zhou, Y.; Robertson, L. A.; Zhang, J.; Shi, Z.; Bheemireddy, S. R.; Shkrob, I. A.; Y, Z.; Li, T.; Zhang, Z.; et al. Unexpected Electrochemical Behavior of an Anolyte Redoxmer in Flow Battery Electrolytes: Solvating Cations Help to Fight against the Thermodynamic−Kinetic Dilemma. *J. Mater. Chem. A* **2020**, *8*, 13470−13479.
(11) Burgess, M.; Hernández-Burgos, K.; Simpson, B. H.; Lichtenstein, T.; Avetian, S.; Nagarjuna, G.; Cheng, K. J.; Moore, J. S.; Rodríguez-López, J. Scanning Electrochemical Microscopy and Hydrodynamic Voltammetry Investigation of Charge Transfer Mechanisms on Redox Active Polymers. *J. Electrochem. Soc.* **2016**, *163*, H3006−H3013.
(12) Watkins, T. S.; Sarbapalli, D.; Counihan, M. J.; Danis, A. S.; Zhang, J.; Zhang, L.; Zavadil, K. R.; Rodríguez-López, J. A Combined SECM and Electrochemical AFM Approach to Probe Interfacial Processes Affecting Molecular Reactivity at Redox Flow Battery Electrodes. *J. Mater. Chem. A* **2020**, *8*, 15734−15745.
(13) Gossage, Z. T.; Schorr, N. B.; Hernandez-Burgos, K.; Hui, J.; Simpson, B. H.; Montoto, E. C.; Rodriguez-Lopez, J. Interrogating Charge Storage on Redox Active Colloids Via Combined Raman Spectroscopy and Scanning Electrochemical Microscopy. *Langmuir* **2017**, *33*, 9455−9463.
(14) Nichols, R. J. Molecular Electronics at Electrode−Electrolyte Interfaces. *Curr. Opin. Electrochem.* **2021**, *25*, No. 100650.
(15) Xiao, X.; Brune, D.; He, J.; Lindsay, S.; Gorman, C. B.; Tao, N. Redox-Gated Electron Transport in Electrically Wired Ferrocene Molecules. *Chem. Phys.* **2006**, *326*, 138−143.
(16) Baghernejad, M.; Zhao, X.; Baruël Ørnsø, K.; Füeg, M.; Moreno-García, P.; Rudnev, A. V.; Kaliginedi, V.; Vesztergom, S.; Huang, C.; Hong, W.; et al. Electrochemical Control of Single-Molecule Conductance by Fermi-Level Tuning and Conjugation Switching. *J. Am. Chem. Soc.* **2014**, *136*, 17922−17925.
(17) Haiss, W. A. T.; van Zalinge, H.; Higgins, S. J.; Bethell, D.; Höhenreich, H.; Schiffrin, D. J.; Nichols, R. J.; Kuznetsov, A. M.; Zhang, J.; Chi, Q.; Ulstrup, J.; et al. Single-Molecule Conductance of Redox Molecules in Electrochemical Scanning Tunneling Microscopy. *J. Phys. Chem. B* **2007**, *111*, 6703−6712.
(18) Kay, N. J.; Higgins, S. J.; Jeppesen, J. O.; Leary, E.; Lycoops, J.; Ulstrup, J.; Nichols, R. J. Single-Molecule Electrochemical Gating in Ionic Liquids. *J. Am. Chem. Soc.* **2012**, *134*, 16817−16826.
(19) Chen, F. H. J.; Nuckolls, C.; Roberts, T.; Klare, J. E.; et al. A Molecular Switch Based on Potential-Induced Changes of Oxidation State. *Nano Lett.* **2005**, *5*, 503−506.
(20) Fatayer, S.; Schuler, B.; Steurer, W.; Scivetti, I.; Repp, J.; Gross, L.; Persson, M.; Meyer, G. Reorganization Energy Upon Charging a Single Molecule on an Insulator Measured by Atomic Force Microscopy. *Nat. Nanotechnol.* **2018**, *13*, 376−380.
(21) Osorio, H. M.; Catarelli, S.; Cea, P.; Gluyas, J. P. G.; Hartl, F.; Higgins, S. J.; Leary, E.; Low, P. J.; Martín, S.; Nichols, R. J.; et al. Electrochemical Single-Molecule Transistors with Optimized Gate Coupling. *J. Am. Chem. Soc.* **2015**, *137*, 14319−14328.
(22) Quinn, J. R.; Venkataraman, L.; Breslow, R.; et al. Oxidation Potentials Correlate with Conductivities of Aromatic Molecular Wires. *J. Am. Chem. Soc.* **2007**, *129*, 12376−12377.
(23) Li, Y.; Wang, H.; Wang, Z.; Qiao, Y.; Ulstrup, J.; Chen, H. Y.; Zhou, G.; Tao, N. Transition from Stochastic Events to Deterministic Ensemble Average in Electron Transfer Reactions Revealed by Single-Molecule Conductance Measurement. *Proc. Natl. Acad. Sci. U.S.A.* **2019**, *116*, 3407−3412.
(24) Milan, D. C.; Al-Owaedi, O. A.; Oerthel, M.; Marqués-González, S.; Brooke, R. J.; Bryce, M. R.; Cea, P.; Ferrer, J.; Higgins, S. J.; Lambert, C. J.; et al. Solvent Dependence of the Single Molecule Conductance of Oligoyne-Based Molecular Wires. *J. Phys. Chem. C* **2016**, *120*, 15666−15674.
(25) Leary, E.; Höbenreich, H.; Higgins, S. J.; van Zalinge, H.; Haiss, W.; Nichols, R. J.; Finch, C. M.; Grace, I.; Lambert, C. J.; McGrath, R.; Smerdon, J.; et al. Single-Molecule Solvation-Shell Sensing. *Phys. Rev. Lett.* **2009**, *102*, No. 086801.
(26) Cao, H.; Ma, J.; Luo, Y.; et al. Temperature-Dependent Statistical Behavior of Single Molecular Conductance in Aqueous Solution. *J. Am. Chem. Soc.* **2008**, *130*, 6674−6675.
(27) Fatemi, V.; Kamenetska, M.; Neaton, J. B.; Venkataraman, L. Environmental Control of Single-Molecule Junction Transport. *Nano Lett.* **2011**, *11*, 1988−1992.
(28) Nováková Lachmanová, S.; Kolivoska, V.; Sebera, J.; Gasior, J.; Meszaros, G.; Dupeyre, G.; Laine, P. P.; Hromadova, M. Environmental Control of Single-Molecule Junction Evolution and Conductance. Case Study of Expanded Pyridinium Wiring. *Angew. Chem., Int. Ed.* **2021**, *60*, 4732−4739.
(29) Bâldea, I. Transition Voltage Spectroscopy Reveals Significant Solvent Effects on Molecular Transport and Settles an Important Issue in Bipyridine-Based Junctions. *Nanoscale* **2013**, *5*, 9222−9230.
(30) Nichols, R. J.; Higgins, S. J. Single Molecule Nanoelectrochemistry in Electrical Junctions. *Acc. Chem. Res.* **2016**, *49*, 2640−2648.
(31) Li, S.; Li, J.; Yu, H.; Pudar, S.; Li, B.; Rodríguez-López, J.; Moore, J. S.; Schroeder, C. M. Characterizing Intermolecular Interactions in Redox-Active Pyridinium-Based Molecular Junctions. *J. Electroanal. Chem.* **2020**, *875*, No. 114070.
(32) Li, B.; Yu, H.; Montoto, E. C.; Liu, Y.; Li, S.; Schwieter, K.; Rodríguez-López, J.; Moore, J. S.; Schroeder, C. M. Intrachain Charge Transport through Conjugated Donor−Acceptor Oligomers. *ACS Appl. Electron. Mater.* **2019**, *1*, 7−12.
(33) Yu, H.; Li, S.; Schwieter, K. E.; Liu, Y.; Sun, B.; Moore, J. S.; Schroeder, C. M. Charge Transport in Sequence-Defined Conjugated Oligomers. *J. Am. Chem. Soc.* **2020**, *142*, 4852−4861.
(34) Li, J.; Shen, P.; Zhen, S.; Tang, C.; Ye, Y.; Zhou, D.; Hong, W.; Zhao, Z.; Tang, B. Z. Mechanical Single-Molecule Potentiometers with Large Switching Factors from Ortho-Pentaphenylene Foldamers. *Nat. Commun.* **2021**, *12*, No. 167.
(35) Zhang, W.; Gan, S.; Vezzoli, A.; Davidson, R. J.; Milan, D. C.; Luzyanin, K. V.; Higgins, S. J.; Nichols, R. J.; Beeby, A.; Low, P. J.; et al. Single-Molecule Conductance of Viologen-Cucurbit[8]Uril Host-Guest Complexes. *ACS Nano* **2016**, *10*, 5212−5220.
(36) Su, T. A.; Neupane, M.; Steigerwald, M. L.; Venkataraman, L.; Nuckolls, C. Chemical Principles of Single-Molecule Electronics. *Nat. Rev. Mater.* **2016**, *1*, No. 16002.
(37) Wang, Y.; Kaur, A. P.; Attanayake, N. H.; Yu, Z.; Suduwella, T. M.; Cheng, L.; Odom, S. A.; Ewoldt, R. H. Viscous Flow Properties and Hydrodynamic Diameter of Phenothiazine-Based Redox-Active Molecules in Different Supporting Salt Environments. *Phys. Fluids* **2020**, *32*, No. 083108.
(38) Qu, X.; Persson, K. A. Toward Accurate Modeling of the Effect of Ion-Pair Formation on Solute Redox Potential. *J. Chem. Theory Comput.* **2016**, *12*, 4501−4508.
(39) Cosimbescu, L.; Wei, X.; Vijayakumar, M.; Xu, W.; Helm, M. L.; Burton, S. D.; Sorensen, C. M.; Liu, J.; Sprenkle, V.; Wang, W. Anion-Tunable Properties and Electrochemical Performance of Functionalized Ferrocene Compounds. *Sci. Rep.* **2015**, *5*, No. 14117.
(40) Robertson, L. A.; Shkrob, I. A.; Agarwal, G.; Zhao, Y.; Yu, Z.; Assary, R. S.; Cheng, L.; Moore, J. S.; Zhang, L. Fluorescence-Enabled Self-Reporting for Redox Flow Batteries. *ACS Energy Lett.* **2020**, *5*, 3062−3068.

https://doi.org/10.1021/acs.jpcc.1c06942
J. Phys. Chem. C 2021, 125, 21862−21872

(41) Peng, L. L.; Chen, F.; Hong, Z. W.; Zhang, J. F.; Fillaud, L.; Yuan, Y.; Huang, M. L.; Shao, Y.; Zhou, X. S.; Chen, J. Z.; et al. Precise Tuning of Single Molecule Conductance in an Electrochemical Environment. *Nanoscale* **2018**, *10*, 7026−7032.
(42) Li, X.; Xu, B.; Xiao, X.; Yang, X.; Zang, L.; Tao, N. Controlling Charge Transport in Single Molecules Using Electrochemical Gate. *Faraday Discuss.* **2006**, *131*, 111−120.
(43) Park, Y. S.; Whalley, A. C.; Kamenetska, M.; Steigerwald, M. L.; Hybertsen, M. S.; Nuckolls, C.; Venkataraman, L. Contact Chemistry and Single-Molecule Conductance: A Comparison of Phosphines, Methyl Sulfides, and Amines. *J. Am. Chem. Soc.* **2007**, *129*, 15768−15769.
(44) Gong, K.; Fang, Q.; Gu, S.; Li, S. F. Y.; Yan, Y. Nonaqueous Redox-Flow Batteries: Organic Solvents, Supporting Electrolytes, and Redox Pairs. *Energy Environ. Sci.* **2015**, *8*, 3515−3530.
(45) Jansen, M. L.; Yeager, H. L. Conductance Study of 1-1 Electrolytes in Propylene Carbonate. *J. Phys. Chem. A* **1973**, *77*, 3089−3092.
(46) Chen, H.; Brasiliense, V.; Mo, Z.; Zhang, L.; Jiao, Y.; Chen, Z.; Jones, L. O.; He, G.; Guo, Q. H.; Chen, X. Y.; et al. Single-Molecule Charge Transport through Positively Charged Electrostatic Anchors. *J. Am. Chem. Soc.* **2021**, *143*, 2886−2895.
(47) Osorio, H. M.; Martín, S.; Milan, D. C.; González-Orive, A.; Gluyas, J. B. G.; Higgins, S. J.; Low, P. J.; Nichols, R. J.; Cea, P. Influence of Surface Coverage on the Formation of 4,4′-Bipyridinium (Viologen) Single Molecular Junctions. *J. Mater. Chem. C* **2017**, *5*, 11717−11723.
(48) Laurinavichyute, V. K.; Nizamov, S.; Mirsky, V. M. The Role of Anion Adsorption in the Effect of Electrode Potential on Surface Plasmon Resonance Response. *ChemPhysChem* **2017**, *18*, 1552−1560.
(49) Glosli, J. N.; Philpott, M. R. Adsorption of Hydrated Halide Ions on Charged Electrodes. Molecular Dynamics Simulation. *J. Chem. Phys.* **1993**, *98*, 9995−10008.
(50) Guo, L. Specific Adsorption of Halide Ions on Iron Surface: A Combined Electrochemical and Monte Carlo Simulation Investigation. *Int. J. Electrochem. Sci.* **2017**, 7064−7074.
(51) Huang, J. C.; Ogrady, W. E.; Yeager, E. The Effects of Cations and Anions on Hydrogen Chemisorption at Pt. *J. Electrochem. Soc.* **1977**, *124*, 1732−1737.
(52) Valette, G. Double Layer on Silver Single-Crystal Electrodes in Contact with Electrolytes Having Anions Which Present a Slight Specific Adsorption: Part I. The (110) Face. *J. Electroanal. Chem. Interfacial Electrochem.* **1981**, *122*, 285−297.
(53) Kamalakannan, S.; Prakash, M.; Chambaud, G.; Hochlaf, M. Adsorption of Hydrophobic and Hydrophilic Ionic Liquids at the Au(111) Surface. *ACS Omega* **2018**, *3*, 18039−18051.
(54) Kondo, H.; Nara, J.; Kino, H.; Ohno, T. Dependence of the Conduction of a Single Biphenyl Dithiol Molecule on the Dihedral Angle between the Phenyl Rings and Its Application to a Nanorectifier. *J. Chem. Phys.* **2008**, *128*, No. 064701.
(55) Vonlanthen, D.; Mishchenko, A.; Elbing, M.; Neuburger, M.; Wandlowski, T.; Mayor, M. Chemically Controlled Conductivity: Torsion-Angle Dependence in a Single-Molecule Biphenyldithiol Junction. *Angew. Chem., Int. Ed.* **2009**, *48*, 8886−8890.
(56) Venkataraman, L.; Klare, J. E.; Nuckolls, C.; Hybertsen, M. S.; Steigerwald, M. L. Dependence of Single-Molecule Junction Conductance on Molecular Conformation. *Nature* **2006**, *442*, 904−907.
(57) Neese, F.; Wennmohs, F.; Becker, U.; Riplinger, C. The Orca Quantum Chemistry Program Package. *J. Chem. Phys.* **2020**, *152*, No. 224108.
(58) Liu, J.; Zhao, X.; Al-Galiby, Q.; Huang, X.; Zheng, J.; Li, R.; Huang, C.; Yang, Y.; Shi, Z.; Manrique, D. Z.; et al. Radical-Enhanced Charge Transport in Single-Molecule Phenothiazine Electrical Junctions. *Angew. Chem., Int. Ed.* **2017**, *56*, 13061−13065.
(59) Funston, A.; Kirby, J. P.; Miller, J. R.; Pospíšil, L.; Fiedler, J.; Hromadová, M.; Gál, M.; Pecka, J.; Valášek, M.; Zawada, Z.; et al. One-Electron Reduction of an "Extended Viologen" P-Phenylene-Bis-4,4′-(1-Aryl-2,6-Diphenylpyridinium) Dication. *J. Phys. Chem. A* **2005**, *109*, 10862−10869.
(60) Burgess, M.; Chénard, E.; Hernández-Burgos, K.; Nagarjuna, G.; Assary, R. S.; Hui, J.; Moore, J. S.; Rodríguez-López, J. Impact of Backbone Tether Length and Structure on the Electrochemical Performance of Viologen Redox Active Polymers. *Chem. Mater.* **2016**, *28*, 7362−7374.
(61) Gadgil, B.; Dmitrieva, E.; Damlin, P.; Ääritalo, T.; Kvarnström, C. Redox Reactions in a Linear Polyviologen Derivative Studied by in Situ Esr/Uv-Vis-Nir Spectroelectrochemistry. *J. Solid State Electrochem.* **2015**, *19*, 77−83.
(62) Li, S.; Yu, H.; Schwieter, K.; Chen, K.; Li, B.; Liu, Y.; Moore, J. S.; Schroeder, C. M. Charge Transport and Quantum Interference Effects in Oxazole-Terminated Conjugated Oligomers. *J. Am. Chem. Soc.* **2019**, *141*, 16079−16084.
(63) Li, S.; Yu, H.; Chen, X.; Gewirth, A. A.; Moore, J. S.; Schroeder, C. M. Covalent Ag-C Bonding Contacts from Unprotected Terminal Acetylenes for Molecular Junctions. *Nano Lett.* **2020**, *20*, 5490−5495.
(64) Yin, X.; Zhang, Y.; Zhu, L.; Low, J. Z.; Liu, Z. F.; Cui, J.; Neaton, J. B.; Venkataraman, L.; Campos, L. M. A Reversible Single-Molecule Switch Based on Activated Antiaromaticity. *Sci. Adv.* **2017**, *3*, No. eaao2615.
(65) Capozzi, B.; Chen, Q.; Darancet, P.; Kotiuga, M.; Buzzeo, M.; Neaton, J. B.; Nuckolls, C.; Venkataraman, L. Tunable Charge Transport in Single-Molecule Junctions Via Electrolytic Gating. *Nano Lett.* **2014**, *14*, 1400−1404.
(66) Izuhara, D.; et al. Poly(Pyridinium Phenylene)S: Water-Soluble N-Type Polymers. *J. Am. Chem. Soc.* **2009**, *131*, 17724−17725.
(67) Tao, N. J. Probing Potential-Tuned Resonant Tunneling through Redox Molecules with Scanning Tunneling Microscopy. *Phys. Rev. Lett.* **1996**, *76*, 4066−4069.
(68) Fujii, S.; Marques-Gonzalez, S.; Shin, J. Y.; Shinokubo, H.; Masuda, T.; Nishino, T.; Arasu, N. P.; Vazquez, H.; Kiguchi, M. Highly-Conducting Molecular Circuits Based on Antiaromaticity. *Nat. Commun.* **2017**, *8*, No. 15984.
(69) Wu, C.; Qiao, X.; Robertson, C. M.; Higgins, S. J.; Cai, C.; Nichols, R. J.; Vezzoli, A. A Chemically Soldered Polyoxometalate Single-Molecule Transistor. *Angew. Chem., Int. Ed.* **2020**, *59*, 12029−12034.
(70) Zhou, P.; Zheng, J.; Han, T.; Chen, L.; Cao, W.; Zhu, Y.; Zhou, D.; Li, R.; Tian, Y.; Liu, Z.; et al. Electrostatic Gating of Single-Molecule Junctions Based on the STM-BJ Technique. *Nanoscale* **2021**, *13*, 7600−7605.
(71) Porter, W. W.; Vaid, T. P. Isolation and Characterization of Phenyl Viologen as a Radical Cation and Neutral Molecule. *J. Org. Chem.* **2005**, *70*, 5028−5035.
(72) Murray, C. A.; Zhu, Z.; Cardin, C. J.; Colquhoun, H. M.; Greenland, B. W. Quadruple Stacking of Macrocyclic Viologen Radical-Cations. *Supramol. Chem.* **2018**, *30*, 751−757.
(73) Chen, H.; Zheng, H.; Hu, C.; Cai, K.; Jiao, Y.; Zhang, L.; Jiang, F.; Roy, I.; Qiu, Y.; Shen, D.; et al. Giant Conductance Enhancement of Intramolecular Circuits through Interchannel Gating. *Matter* **2020**, *2*, 378−389.
(74) Tang, C.; Zheng, J.; Ye, Y.; Liu, J.; Chen, L.; Yan, Z.; Chen, Z.; Chen, L.; Huang, X.; Bai, J.; et al. Electric-Field-Induced Connectivity Switching in Single-Molecule Junctions. *iScience* **2020**, *23*, No. 100770.

https://doi.org/10.1021/acs.jpcc.1c06942
J. Phys. Chem. C 2021, 125, 21862−21872